REVIEW

Check for updates

Metal–organic frameworks for electrocatalytic hydrogen peroxide production

Xinchan Zhang, Chaoqi Zhang, Chengzhong Yu [ID] * and Chao Liu [ID] *

The electrocatalytic two electron oxygen reduction reaction (2e-ORR) has aroused extensive attention as a promising alternative route to the prevailing anthraquinone process for H_2O_2 production, where the design of efficient electrocatalysts with high activity, high selectivity and a high H_2O_2 production rate is the key. Metal–organic frameworks are an emerging class of crystalline porous materials with a high specific surface area, ease of structural control, and evenly distributed and well-defined metal sites. These remarkable features provide MOFs with great potential as high-performance electrocatalysts. To date, several excellent reviews of MOF-based electrocatalysts have been reported in the fields of 4e-ORR, oxygen evolution reaction, hydrogen evolution reaction, CO_2 reduction reaction and nitrogen reduction reaction. However, a dedicated review of 2e-ORRs is still lacking. In this review, we provide an overview of the recent advances in the design of MOF-based 2e-ORR electrocatalysts for H_2O_2 production. The electrocatalytic mechanism and performance evaluation methods of the 2e-ORR is firstly introduced. Then, MOF-based 2e-ORR electrocatalysts including pristine MOFs, MOF composites and MOF derivatives are summarized with the structure–property relationships elucidated. Finally, some current challenges and future perspectives are discussed for the further development of this emerging field.

1. Introduction

Hydrogen peroxide (H_2O_2) is a versatile and ecofriendly oxidant with a wide range of applications in textile bleaching,[1] wastewater purification,[2,3] disinfection,[4] chemical synthesis[5] and fuel cells.[6] Currently, the anthraquinone process is predominately used for the industrial production of H_2O_2,[7] which

School of Chemistry and Molecular Engineering, East China Normal University, Shanghai 200241, P. R. China. E-mail: cliu@chem.ecnu.edu.cn, czyu@chem.ecnu.edu.cn

requires large-scale infrastructures, complex operations, high storage and transportation costs, and generates substantial hazardous waste products. The direct synthesis of H_2O_2 from hydrogen and oxygen offers a more straightforward route.[8,9] In this process, high temperature and pressure, and noble-metal catalysts are required, which create a serious explosion risk, limiting its practical application.[10] As a promising alternative to the prevailing anthraquinone method and direct synthesis process, the electrochemical two-electron oxygen reduction reaction (2e-ORR) using O_2 and H_2O as raw materials has

Xinchan Zhang is currently a master's student under the supervision of Prof. Chengzhong Yu and Prof. Chao Liu at East China Normal University. Her research field is MOF-based nanomaterials for applications in electrocatalysis.

Xinchan Zhang

Chaoqi Zhang received his PhD degree in Chemistry from East China Normal University in 2022 and now works as a postdoctoral fellow in Chengzhong Yu's group at East China Normal University. His research focuses on the design and application of advanced electrocatalysts.

Chaoqi Zhang

attracted rapidly increasing attention for decentralized H_2O_2 production due to the advantages of mild reaction conditions, easy operation and environmental friendliness.[11,12] The key to success for the 2e-ORR is the design and synthesis of highly efficient electrocatalysts, which selectively reduce O_2 into H_2O_2, rather than H_2O via the competitive 4e-ORR pathway.

Recent extensive studies have led to the discovery of various 2e-ORR electrocatalysts including noble metals and their alloys,[13] carbon materials,[14,15] single atom catalysts,[16] transition-metal compounds and metal–organic frameworks.[17] Noble metals are generally high-performing with a small overpotential and high selectivity for the 2e-ORR,[18] however, their scarcity and high cost prevent their large-scale application.[19] In carbon-based materials with a high abundance and low cost, the activity is mainly stemmed from defect engineering and heteroatom doping, where the task specific structure design with atomic precision is difficult.[20] Different from carbon-based materials, transition metal compounds exhibit easily identifiable and controllable active sites.[21] Nevertheless, the agglomerate form with a low surface area and poor porosity limits the accessibility and utilization of internal active sites.[22] Even the construction of isolated sites can significantly improve the atomic utilization and 2e-ORR selectivity, and the content of active phases in most single-atom catalysts is extremely low with an unsatisfactory H_2O_2 yield.

Metal–organic frameworks (MOF), composed of metal ions/clusters and organic ligands, are an important class of crystalline porous materials with remarkable features including a large specific surface area, regular and controllable pore structures, and diversity in chemical compositions and functionality.[23–26] The uniformly distributed and precisely determined metal centers are separated by ligands, making MOFs intrinsically[27] "single-atom" catalysts with high-content isolated active centers. The chemical reaction environments and electronic structures of active centers can be rationally customized for specific applications by changing the types of ligands and/or metal node.[28,29] The high porosity further promotes the exposure and accessibility of active sites and accelerates the mass transfer within the network of MOFs.[30,31] In addition, the hybridization of other functional materials with MOFs results in multifunctional composite materials with integrated properties. When used as sacrificial templates, MOFs can also be converted into various nanostructures including porous carbon,[32] metal compounds,[33] and their composites, generally with enhanced stability and conductivity. In view of these unique merits, MOF-based materials have emerged as promising 2e-ORR electrocatalysts for H_2O_2 production.

For MOF-based electrocatalysts, several excellent reviews have been contributed regarding the 4e-ORR,[34] oxygen evolution reaction,[35] hydrogen evolution reaction,[36] electrochemical CO_2 reduction reaction[37] and nitrogen reduction reaction.[38] However, a review of MOF-based electrocatalysts dedicated to the 2e-ORR is still lacking. Considering the impressive advances in this emerging but fast-growing field over the past few years, a timely review on the design and application of MOF-based 2e-ORR electrocatalysts for H_2O_2 production is of great significance and is highly desired.

In this review, an overview on the latest progress of MOF-based electrocatalysts for the 2e-ORR toward H_2O_2 production is provided (Scheme 1). Firstly, the catalytic mechanisms of the 2e-ORR with existing methods for performance evaluation will be briefly introduced. Secondly, particular attention will be paid to the construction of MOF-based 2e-ORR materials including pristine MOFs, MOF composites and MOF derivatives, with the design principles and structure–property relationship highlighted. Lastly, a discussion on the challenges and prospects of the design and application of MOFs for H_2O_2 electrosynthesis will be presented, aiming to stimulate widespread interest in further development of MOFs for H_2O_2 production.

2. Catalytic mechanism and methods for performance evaluation of the 2e-ORR

2.1 Catalytic mechanism of the 2e-ORR

The oxygen reduction reaction involves a multi-step electron transfer process with two kinds of reaction pathways. The first is the long-standing 4e$^-$ electrochemical reduction of O_2 into H_2O under acid/neutral conditions (eqn (1a)–eqn (1d)) or OH$^-$

Chengzhong Yu received his PhD degree in Chemistry from Fudan University (China) in 2002 and then worked as a professor at Fudan University until 2010. He is currently a professor at the University of Queensland (Australia) and East China Normal University. His research focuses on nanoporous materials and nanostructured composites for applications in biotechnology, clean energy, and environmental protection.

Chengzhong Yu

Chao Liu received his Bachelor (2012) and PhD degrees (2018) at Nanjing University of Science and Technology. He worked as a postdoctoral fellow in Prof. Chengzhong Yu's group at East China Normal University (2018–2021). He is currently a professor at East China Normal University. His research focuses on the design and synthesis of nanostructured MOF materials for catalysis.
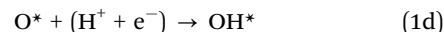
Chao Liu
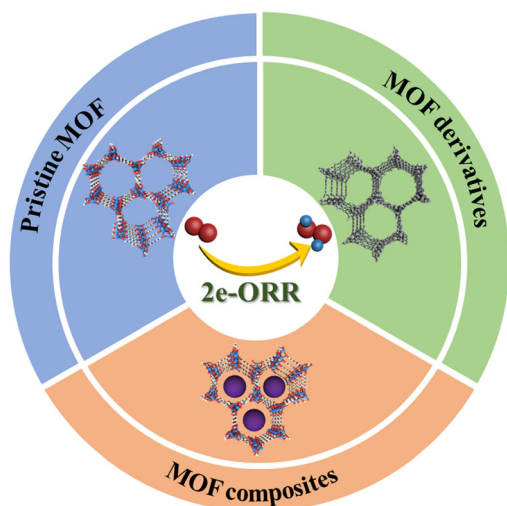
Scheme 1 An overview of the structures and applications of MOF-based 2e-ORR electrocatalysts.

under alkaline conditions (eqn (2a)–eqn (2d)), comprising four elementary steps with three reaction intermediates of *OOH, *O and *OH.[39] The 2e-associative pathway, relating to O_2 reduction into H_2O_2 under acid/neutral conditions (eqn (3a)–eqn (3c)) or OOH^- under alkaline conditions (eqn (4a)–eqn (4c)), experiences two coupled electron-proton transfer steps with only one reaction intermediate (OOH*).[40,41] Scheme 2 shows a schematic diagram of the ORR mechanism. Once the OOH* species are formed, there are three possible subsequent pathways: (1) desorption into the electrolyte as the final product; (2) further reduction into OH^- *via* O–O bond cleavage; and (3) chemical decomposition into O_2 and OH^-. Due to the thermodynamic preference for H_2O as the end product, the selectivity of the $2e^-$ pathway over the catalysts for H_2O_2 synthesis is a great challenge.[42]
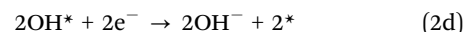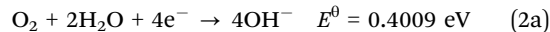
4e-ORR under acidic/neutral conditions (pH $\leqslant$ 7):

$$O_2 + 4(H^+ + e^-) \rightarrow 2H_2O \quad E^\theta = 1.23 \text{ eV } vs. \text{ RHE} \quad (1a)$$
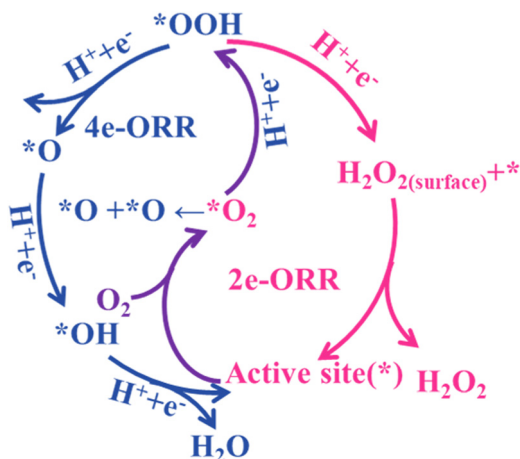
Scheme 2 Schematic diagram of the ORR mechanism.

$$* + O_2 + (H^+ + e^-) \rightarrow OOH^* \quad (1b)$$

$$OOH^* + (H^+ + e^-) \rightarrow H_2O + O^* \quad (1c)$$

$$O^* + (H^+ + e^-) \rightarrow OH^* \quad (1d)$$

4e-ORR under alkaline conditions (pH > 7):

$$O_2 + 2H_2O + 4e^- \rightarrow 4OH^- \quad E^\theta = 0.4009 \text{ eV} \quad (2a)$$

$$2* + O_2 \rightarrow 2O^* \quad (2b)$$

$$2O^* + 2H_2O + 2e^- \rightarrow 2OH^- + 2OH^* \quad (2c)$$

$$2OH^* + 2e^- \rightarrow 2OH^- + 2* \quad (2d)$$

2e-ORR under acidic/neutral conditions (pH $\leqslant$ 7):

$$O_2 + 2(H^+ + e^-) \rightarrow H_2O_2 \quad E^\theta = 0.7 \text{ eV } vs. \text{ RHE} \quad (3a)$$

$$* + O_2 + (H^+ + e^-) \rightarrow OOH^* \quad (3b)$$

$$OOH^* + (H^+ + e^-) \rightarrow H_2O_2 + * \quad (3c)$$

2e-ORR under alkaline conditions (pH > 7):

$$O_2 + H_2O + 2e^- \rightarrow HO_2^- + OH^- \quad (4a)$$

$$* + O_2 + H_2O + e^- \rightarrow OOH^* + OH^- \quad (4b)$$

$$OOH^* + e^- \rightarrow HO_2^- + * \quad (4c)$$
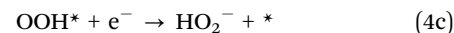
Toward a high 2e-selectivity, the customized adsorption mode of O_2 is crucial. Generally, the 'end-on' adsorption mode favors the 2e-ORR pathway by restricting the cleavage of the O–O bond. In contrast, the 'side-on' adsorption configuration can promote the breaking of O–O bonds through the cooperation of neighboring active sites, inducing a 4e-process.[43,44] Moreover, the absorption strength of OOH* on active sites should be appropriate, neither too strong nor too weak.[45] In the case of a too weak interaction, O_2 protonation and the formation of an OOH* intermediate is prevented, resulting in limited activity and selectivity. However, a too strong interaction is conducive for the competitive 4e-ORR. Furthermore, the protonation of O_2 and desorption of H_2O_2 can also regulate the 2e-ORR activity and selectivity. For example, the latest advance showed that the participation of water could facilitate the protonation of OOH* as the proton source in alkaline electrolyte and further promote the leave of H_2O_2, leading to higher 2e-ORR selectivity and H_2O_2 yield.[46]

2.2 Methods for the performance evaluation of 2e-ORR

The performance evaluation of 2e-ORR activity and selectivity in laboratory research relies on the rotating-ring disk electrode (RRDE) technique. During the RRDE test, an oxygen reduction reaction first occurs at the catalyst-coated disk electrode to generate both H_2O_2 and H_2O. Under the convection forces from the rotation of the electrode, the H_2O_2 is diffused to the ring electrode and subsequently oxidized back to O_2. By analysing the currents of the disk (I_d) and ring (I_r) electrodes, the

2e-selectivity towards H_2O_2 can be assessed using the equation:

$$H_2O_2\% = \frac{200 I_r}{(N \times I_{d+} I_r)}.$$

From the LSV (linear sweep voltammetry) curves, the onset potential that represents the lowest potential to drive the ORR and overpotential that refers to the difference between theoretical thermodynamic potential and the potential reaching a given current can also be determined. If the overpotential is close to zero, sometimes it is called the 'zero overpotential'.[47,48] The electron transfer number (n) can also be calculated using the equation:[49]

$$n = \frac{4 \times I_d}{I_r \times N}$$

where N is the current collection efficiency of the Pt ring electrode.

The H_2O_2 production faradaic efficiency (FE) can be calculated by dividing the charge transferred to the produced H_2O_2 by the total charge passed through the circuit using the equation:[49]

$$H_2O_2:FE = \frac{2 \times C \times V \times F}{Q}$$

Here, C is the H_2O_2 concentration (mol L^{-1}), V means the volume of electrolyte (L), F represents the Faraday constant (96 485 C mol^{-1}), and Q is the amount of charge passed (C).

As a key indicator of reaction kinetics, the Tafel slope can also be calculated according to LSV curves using the equation:

$$\eta = a + b \log(j) \left(a = 2.303 RT \frac{\log j_0}{\alpha n F} \right)$$

where b refers to the Tafel slope, j is the current density, R denotes the ideal gas constant, T is the absolute temperature, j_0 represents the exchange current density, F stands for the Faraday constant and α means the charge transfer coefficient.

To determine the production rate of H_2O_2, an H-type electrolytic cell is usually used and the concentration of H_2O_2 in the reaction solution can be measured using the most widely used cerium sulfate $Ce(SO_4)_2$ titration method. The mechanism is that the yellow solution of Ce^{4+} can be reduced to colorless Ce^{3+} by H_2O_2:

$$2Ce^{4+} + H_2O_2 \rightarrow 2Ce^{3+} + 2H^+ + O_2$$

The Ce^{4+} concentration can be determined by ultraviolet-visible spectroscopy at usually 316 nm. The concentration of $C(H_2O_2)$ can thus be calculated using the following equation:

$$C(H_2O_2) = 2C(Ce^{4+})$$

where $C(Ce^{4+})$ refers to the moles of consumed Ce^{4+}.

Additionally, the iodometric titration method is also useful for determining the concentration of H_2O_2. A typical protocol is that a certain amount of the reaction solution obtained from the electrochemical system is added to a mixture of potassium hydrogen phthalate ($C_8H_5KO_4$) and potassium iodide (KI)

aqueous solution. The mixed solution is allowed to react for 30 minutes, where the H_2O_2 molecules react with I^- to produce I_3^- using the following equation:

$$H_2O_2 + I^- \rightarrow I^{3-} + H_2O$$
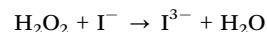
The amount of I_3^- was measured by ultraviolet-visible spectroscopy or a microplate reader under the wavelength of 350 nm. The concentration of H_2O_2 can be determined using the following equation:[14]

$$C(H_2O_2) = C(I_3^-)$$

where $C(I_3^-)$ represents the quantity of I_3^- consumed in moles.

Titanium salt colorimetry is another effective method for H_2O_2 detection.[18] Typically, a TiO^{2+} ion solution is prepared by dissolving titanium dioxide and ammonium sulfate in concentrated sulfuric acid. Then, the H_2O_2 contained electrolyte is added into the above TiO^{2+} ion solution. After reaction for 10 min, the H_2O_2 molecules oxidize the colourless TiO^{2+} ions into yellow $[TiO(H_2O_2)]^{2+}$ ions. The concentration of $[TiO(H_2O_2)]^{2+}$ ions can be measured by ultraviolet-visible spectroscopy at 430 nm for quantification of H_2O_2.

The stability of an electrocatalyst can be evaluated using two common approaches, including chronoamperometry (I–t curve at a constant potential) and chronopotentiometry (E–t curve at a fixed current density). For 2e-ORRs, high stability is reflected by a consistent current density at a fixed potential through chronoamperometry or negligible overpotential increase at a fixed current density by chronopotentiometry.

3. MOF-based 2e-ORR electrocatalysts

3.1 Pristine MOFs

3.1.1 Monometallic MOFs. Given the aforementioned structural advantages, pristine MOFs have shown great potential as 2e-ORR electrocatalysts. To achieve high performance, the current efforts have been mainly devoted to the electronic structure regulation of MOFs *via* metal doping, ligand design, defect engineering and facet control to selectively reduce O_2 into H_2O_2.[50,51] Furthermore, the nanostructure design that may greatly affect the active site accessibility, and electron and mass transfer is also crucial.

For example, Ren and co-workers explored the ORR performance of Prussian blue analogues (PBAs) with different metal centers including Co, Ni, Zn, and Cu (Fig. 1(a)).[52] The transmission electron microscope (TEM) images of Zn-PBAs as a typical sample showed porous structures with a lattice space of 2.4 Å assigned to the (420) planes (Fig. 1(b) and (c)). Among all samples, Zn-PBAs exhibited the best 2e-ORR performance with an average electron-transfer number of 2.3–2.5 and a H_2O_2 selectivity of 88% at 0 V *vs.* RHE (Fig. 1(d) and (e)). Density functional theory (DFT) calculations indicated the energetically unfavorable formation of O* on the Zn site with a prevented 4e$^-$ but preferred 2e$^-$ pathway (Fig. 1(f)).
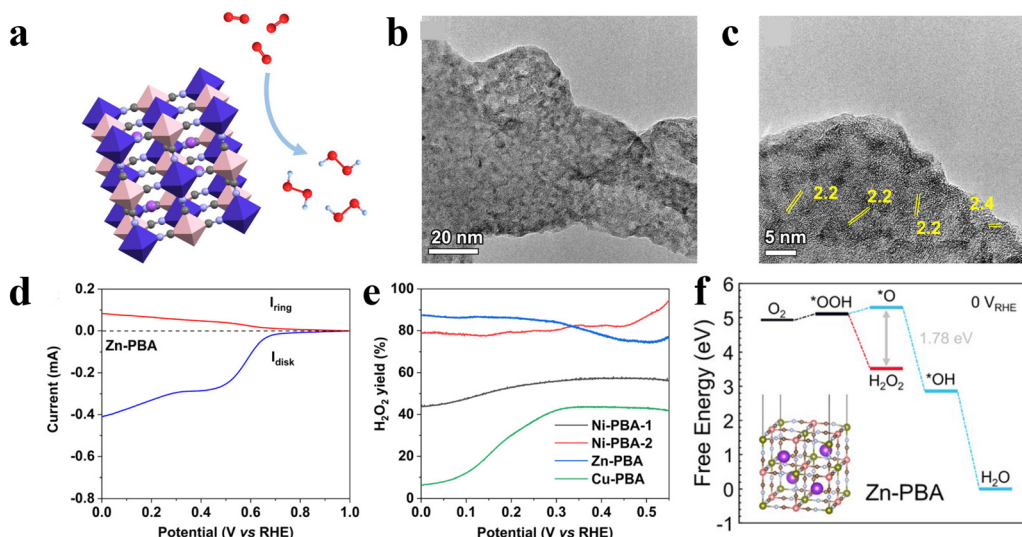
Fig. 1 (a) Illustration of the M-PBA structure. (b) and (c) TEM images of the Zn-PBA catalysts. (d) LSV curves, (e) selectivity of Zn-PBA, and (f) free-energy diagrams for the ORR on Zn-PBA. Copyright 2022, American Chemical Society.

Except for the types of metal centers, the design of unsaturated coordinated metal sites (UCMSs) in MOFs for the 2e-ORR was reported by Huang and co-workers.[16] In their work, a novel liquid–liquid interfacial reaction method was developed for the synthesis of 2D (two dimension) Ni MOF NSs using terephthalic acid (1,4-H_2BDC) as the ligand and Ni^{2+} as metal ions (Fig. 2(a)). The amounts of UCMSs were precisely tuned via simply changing the ratios of metal precursors and organic linkers ($R_{M/L}$) from 2, 4, and 6 to 8, and the corresponding samples were denoted as Ni MOF NS-2, 4, 6 and 8, respectively. All the materials possessed a 2D nanosheet structure with a parallelogram-like shape (Fig. 2(b) and (c)). The lateral dimensions and thickness were measured to be ≈ 200–450 and 5 nm, respectively. The electrochemical results (Fig. 2(d) and (e)) showed that the selectivity of H_2O_2 increased first and then decreased with the increase of $R_{M/L}$ with the contrary trend of electron transfer number (Fig. 2(f)). Ni MOF NS-6 with the $R_{M/L}$ of 6 exhibited the most positive near-zero overpotential, H_2O_2 selectivity of 98% and H_2O_2 production rate of 80 mmol g_{cat}^{-1} h^{-1} in 0.1 M KOH. The X-ray absorption fine structure (XAFS) spectroscopy displayed the highest Ni^{2+}/Ni^{3+} atomic ratio in Ni MOF NS-6 among all samples, which was beneficial to the
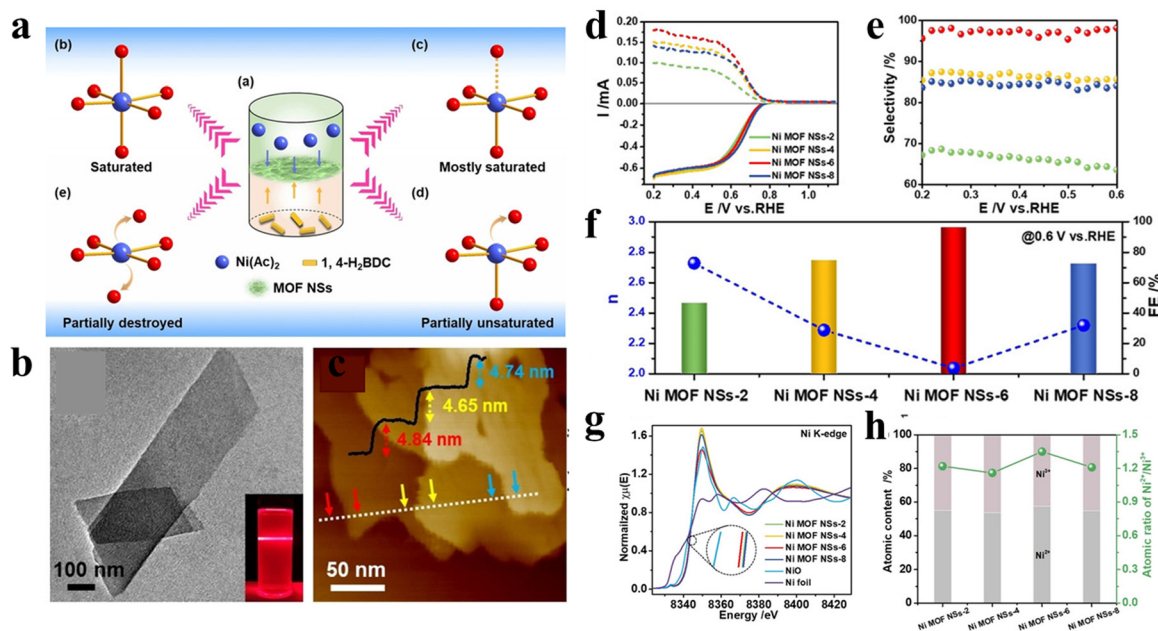
Fig. 2 (a) Illustration of the synthetic method for Ni MOF NSs. (b) TEM and (c) AFM images of Ni–MOF NS-6. (d) LSV curves and (e) H_2O_2 selectivity. (f) The number of electrons transferred (n) and the Faraday efficiency. (g) XANES spectra for Ni MOF NS-2, 4, 6, 8, NiO and Ni foil. (h) The atomic content of Ni^{2+} and Ni^{3+}, and the atomic ratio of Ni^{2+}/Ni^{3+} in Ni MOF NS-2, 4, 6 and 8. Copyright 2021, WILEY-VCH.

formation of OOH*(Fig. 2(g) and (h)). Together with the highest micropore volume that is conducive for mass diffusion, an enhanced 2e-ORR performance of Ni MOF NS-6 was achieved.

Beyond traditional MOFs with low conductivity, the emerging conductive metal–organic frameworks (cMOFs) with a π-conjugated structure and enhanced conductivity have also been utilized as 2e-ORR electrocatalysts. For instance, Sun et al. compared the 2e-ORR performances of several typical conductive MOFs with different metal centers (Ni or Cu) and oxidative organic linkers HHTP or HITP (HHTP = 2,3,6,7,10,11-triphenylenehexol or HITP = 2,3,6,7,10,11-hexaaminotriphenylen).[53] As shown in Fig. 3(a), the optimized sample of Cu-HHTP exhibited a nanorod-like morphology with a length of ≈ 100 nm. An excellent 2e-ORR performance with a high H_2O_2 selectivity of 95% and superior H_2O_2 yield rate of 792.7 mmol g_{cat}^{-1} h^{-1} was delivered by Cu-HHTP in 0.1 M KOH (Fig. 3(b)–(d)), outperforming Cu-HITP (71%, ~ 293.2 mmol g_{cat}^{-1} h^{-1}) and Ni-HITP (39%, ~ 157.3 mmol g_{cat}^{-1} h^{-1}). To explore the origin of the enhanced performance, in situ XAFS measurement was performed. In Cu-HHTP, the dynamic coupling of hydroxyl groups over Cu sites could effectively induce the self-polarization of the π-conjugated metal–ligand Cu–O–C site (Fig. 3(e)–(f)), facilitating the generation of the key immediate of OOH*. The dynamic process of the self-polarization and the evolution of Cu sites is depicted in Fig. 3(g).

Furthermore, the confinement of halogen anions into the nanocavity of cMOF was reported to enhance the H_2O_2 selectivity by Liu and colleagues.[54] Through the introduction of various ammonium halides during the solvothermal reaction process, X-Ni MOFs (X = F, Cl, Br, or I) with a microfold flower-like structure were synthesized through a facile ion confinement strategy. Compared to other halogen anion (i.e. F, Cl and I) modified samples, the Br–Ni MOF delivered better 2e-ORR performances with a selectivity of 90%, a H_2O_2 faradaic efficiency (FE) of 86% and a H_2O_2 yield rate of 596 mmol g_{cat}^{-1} h^{-1}. The enhanced performance was ascribed to the inhibited dissociation of critical *OOH intermediates by introducing Br, as evidenced by the operando XAFS and Fourier transform infrared (FTIR) spectra.

Considering the instability of H_2O_2 under alkaline conditions, the production of H_2O_2 in neutral or acidic solution is desired. Within this context, Dominic Ross et al.[55] prepared a 2D-MOF, Ni_3HAB_2 (HAB = hexaaminobenzene) for H_2O_2 production in 0.1 M PBS (pH = 6.5–6.6) with a selectivity of 90% and H_2O_2 yield of 662 ppm (Fig. 4(a)). Operando XAS (X-ray absorption spectra) suggested that the charging of HAB induced a dynamic Ni oxidation state under an Ar atmosphere, while under O_2-saturated conditions, the structure of Ni_3HAB_2 slightly changed with oxygen-containing species strongly adsorbed at potentials more negative than the reduction potential of HAB (E_{redox} of ~ 0.3 V vs. RHE) (Fig. 4(b)). The authors hypothesized that a 2e-ORR dominant mechanism took place on HAB when $E > E_{redox}$, but H_2O_2 production could also be triggered by Ni-mediated linker discharge when $E < E_{redox}$ (Fig. 4(c)).

Aside from common Ni-based MOFs, Dong et al.[56] designed two-dimensionally layered conductive $Mg_3(HITP)_2$ using a solvothermal process (Fig. 5(a)), exhibiting a 2D regular hexagonal structure with a pore size of 2.25 nm (Fig. 5(b)). The near zero ELF values of the Mg atom revealed the existence of ionic bonding in Mg–N bonds. The (II) valence Mg active site with a
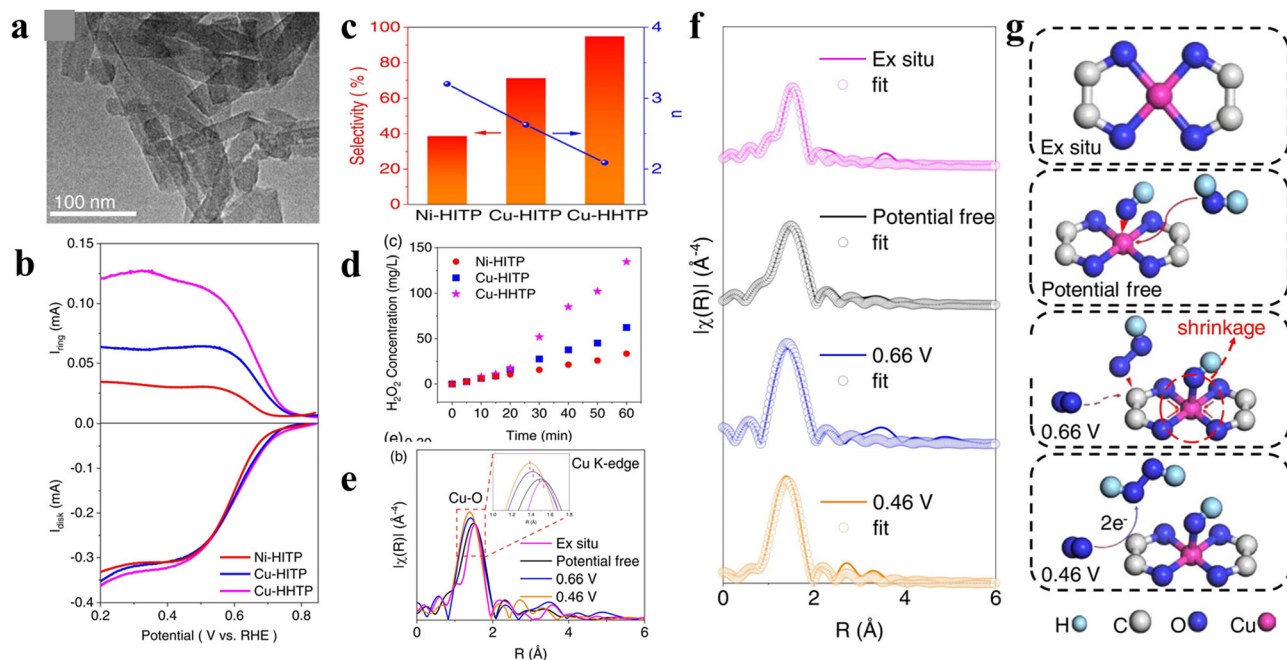

Fig. 3 (a) TEM image of Cu-HHTP. (b) LSV curves. (c) H_2O_2 selectivity and the electron transfer number of Ni-HITP, Cu-HITP and Cu-HHTP. (d) Cumulative H_2O_2 yield. (e) FT-XAFS curves for Cu-HHTP. (f) The FT-XAFS fitting results of Cu-HHTP. (g) Scheme of the proposed 2e ORR mechanism for Cu-HHTP. Copyright 2022, Elsevier.
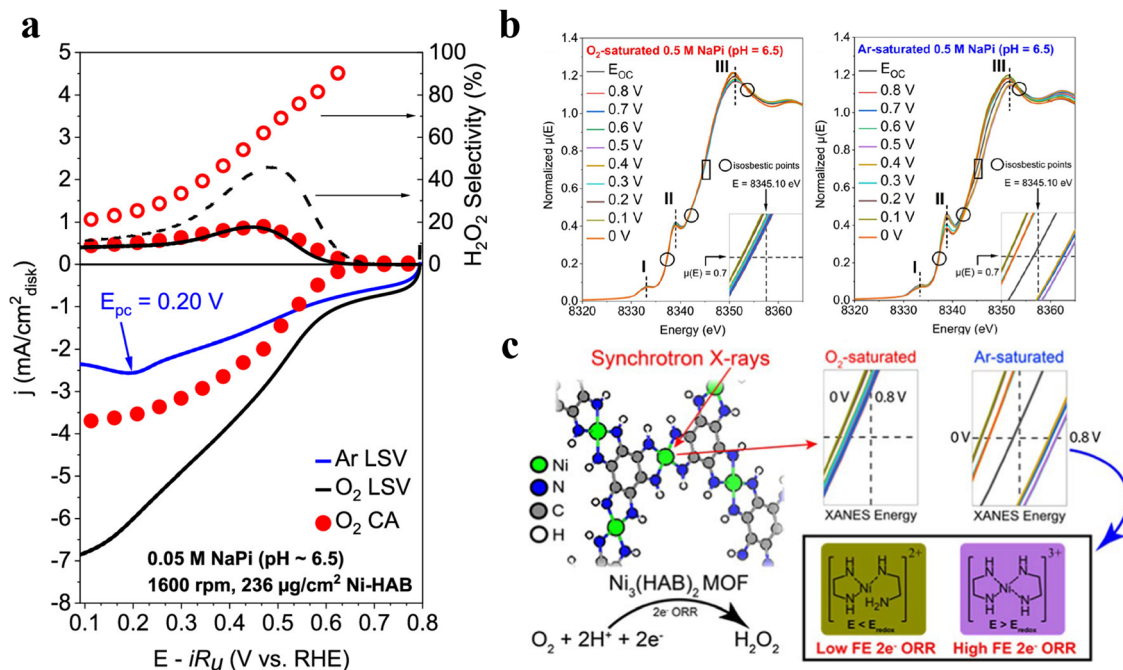
Fig. 4 (a) LSV curves of Ni-HAB. (b) XANES spectra of Ni-HAB/CFP at various applied potentials in O_2 saturated and Ar saturated electrolytes. (c) Schematic illustrating the changes in the nickel oxidation state during the 2e-ORR process. Copyright 2022, American Chemical Society.

highly positive charge and low oxygen affinity could promote the adsorption of OOH*, resulting in 2e-ORR being the dominant reaction pathway (Fig. 5(f)–(h)). Additionally, the π–π stacking between organic moieties and conductive electrolyte ions enabled the fast charge transportation between layers. As a consequence, the $Mg_3(HITP)_2$ demonstrated a high selectivity of >90%, a H_2O_2 yield up to 3400 ppm and excellent stability in 0.1 M PBS (Fig. 5(c)–(e)). *In situ* spectroscopic further suggested the formation of key intermediate OOH* on the Mg^{2+} active site.
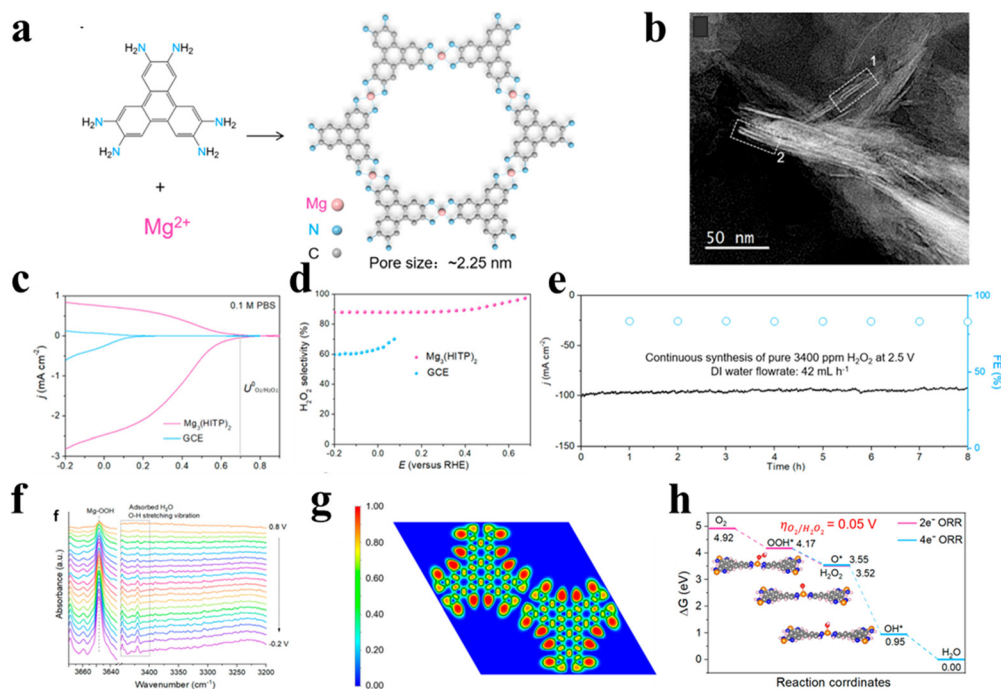
Fig. 5 (a) Diagram of the structure of $Mg_3(HITP)_2$. (b) STEM image of $Mg_3(HITP)_2$. (c) LSV curves of $Mg_3(HITP)_2$. (d) H_2O_2 selectivity. (e) Stability test. (f) *In situ* ATR-IR spectra of $Mg_3(HITP)_2$ under applied potentials. (g) The electron localization function distribution of the $Mg_3(HITP)_2$ monolayer. (h) Free energy diagrams for $2e^-$ (red line) and $4e^-$ (cyan line) ORR processes. Copyright 2022, American Chemical Society.

1090 | *Mater. Chem. Front.*, 2024, **8**, 1084–1100

This journal is © The Royal Society of Chemistry and the Chinese Chemical Society 2024

3.1.2 Bimetallic MOFs. Compared to the aforementioned mono-metal MOFs, the construction of bimetallic MOFs can further improve the 2e-ORR performance with a modulated electronic structure through the synergistic effect of different metals. As a typical example, Liu et al.[57] reported the synthesis of a series of cMOFs with Ni–M (M = Co, Cu, Zn) bimetal centers as 2e-ORR electrocatalysts. Among them, NiZn MOF with a nanosheet assembled structure (Fig. 6(a)) exhibited the best 2e-ORR performance with a selectivity of up to 90% in the 2e-ORR process, higher than that of the NiCo (45%) and NiCu (55%) counterparts (Fig. 6(b) and (c)). Synchrotron radiation-FTIR (SR-FTIR) spectroscopy was used to show that the NiZn MOF with dominant Ni^{3+} could effectively enhance and stabilize the absorption of crucial *OOH intermediates on its active sites (Fig. 6(d)–(f)) and XAFS observations verified that the electron interactions between the Ni 3d orbital and the Zn^{2+} ions connected by HITP ligands promoted the oxidation of Ni from +2 to $+(2 + \delta)$ ($0 < \delta < 1$), enabling an appropriate adsorption energy of *OOH intermediates for promoting the 2e-ORR (Fig. 6(g)–(i)).

Except for only adjusting the metal centers, Zhang and co-workers[40] have simultaneously manipulated the structure of MOFs at both the atomic and nano-scale to further improve the catalytic performance using the well-known ZnCo-ZIF as a model catalyst. The electronic structure of Co centers was precisely adjusted by altering the molar ratio of Zn/Co with the exposed facets controlled by using cetyltrimethylammonium bromide (CTAB) as a modulator (Fig. 7(a)). With the increase of Zn/Co, the selectivity of H_2O_2 first increased and then decreased for the (001) dominated ZnCo-ZIF nanocube (Fig. 7(b)). The optimized sample with the Zn/Co ratio of 9/1 (ZnCo-ZIF-C_3) exhibited a satisfactory 2e-ORR catalytic performance, with a selectivity of ∼100%, H_2O_2 yield of 4.35 mol g_{cat}^{-1} h^{-1} and FE of ∼95% in 0.1 M KOH. When used in 0.1 M PBS, a high selectivity of 92%, FE of ∼90% and H_2O_2 yield of 3.8 mol g_{cat}^{-1} h^{-1} were also delivered by ZnCo-ZIF-C_3 (Fig. 7(c) and (d)). Compared to the (110) exposed ZnCo-ZIF-R_3, ZnCo-ZIF-C_3 showed significantly enhanced performances. The experimental and theoretical results indicated that the Zn doping triggered the electron insufficient state of the Co center toward the optimized adsorption ability of the OOH* intermediate, leading to the high selectivity (Fig. 7(e)). Moreover, a unique role of water binding to Co acting as a "nucleophile" during the 2e-ORR process was unveiled, which promoted the protonation of OOH* and desorption of HOOH (Fig. 7(f)–(i)).

Even though great advances have been achieved in pristine MOF-based 2e-ORR electrocatalysts, their relatively low stability, poor conductivity and micropore-dominated structure seriously hinder their further development. Therefore,
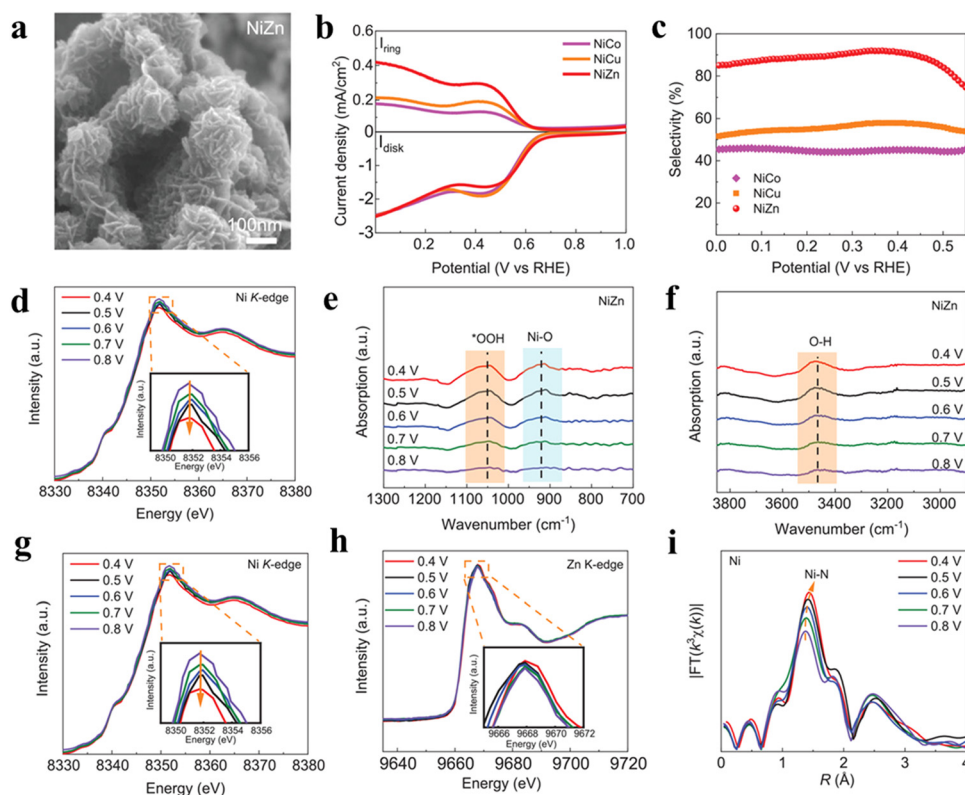
Fig. 6 (a) SEM image of NiZn MOF. (b) LSV curves of NiM MOF catalysts. (c) H_2O_2 selectivity. In situ SR-FTIR spectra in the wavenumber range of (d) 700–1300 cm^{-1} and (e) 2900–3850 cm^{-1} under various potentials for the NiZn MOF catalyst. (f) Infrared signals at 1050 and 3480 cm^{-1} versus the potential for NiZn MOF. (g) In situ Ni K-edge. (h) Zn K-edge XANES spectra of NiZn MOF during the ORR. (i) Corresponding in situ Ni K-edge EXAFS spectra for NiZn MOF at different applied potentials. Copyright 2022, Wiley.

Fig. 7 (a) Illustration of (a) ZnCo-ZIF based 2e-ORR electrocatalysts with different Zn/Co ratios and crystal facet exposure. (b) SEM image of ZnCo-ZIF-C_3. (c) H_2O_2 production rate of all samples in 0.1 M PBS. (d) H_2O_2 production rate of all samples in 0.1 M KOH. (e) Relationship between selectivity and d-band center for different catalysts. (f), (g) free energy profiles of the ORR reaction path on ZnCo-ZIF-C_3 and ZIF-67, and (h), (i) optimized structures of the reaction intermediates on the ZIF-67 (001) surface, and the ZnCo-ZIF-C_3 (001) surface. Copyright 2023, American Chemical Society.

elaborate structural design of pristine MOF-based 2e-ORR electrocatalysts to increase the bonding strength of metal–ligand coordination, introduce conducting units and create meso/macro-pores deserves significant research efforts.
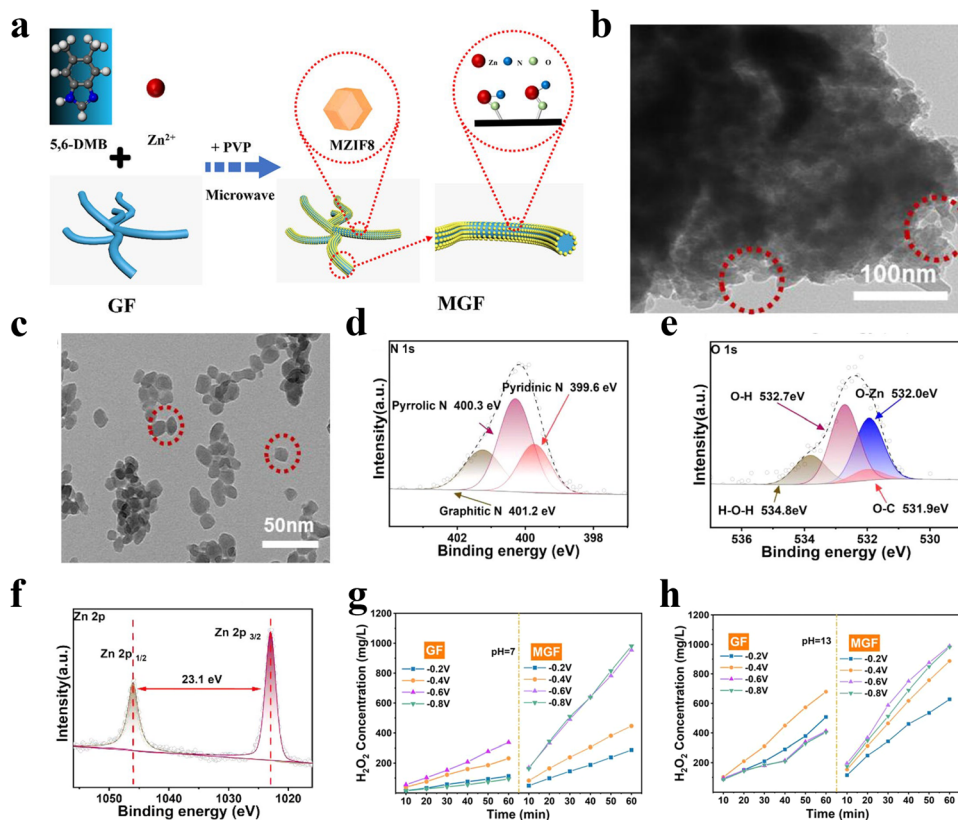
3.2 MOF composites

Beyond single-component pristine MOFs, the construction of MOF composites by integrating MOFs with other functional materials is an efficient strategy to further improve the properties of MOFs. Even though MOF composites have been investigated in widespread applications and shown enhanced performances such as in the 4e-oxygen reduction reaction,[29] hydrogen evolution reaction[58] and oxygen evolution reaction,[59] their application in the 2e-ORR is much rarer.

One typical example is the combination of CoTCPP (5,10,15,20-tetrakis-(4-carboxlatophenyl)-porphyrin-cobalt(III) chloride) with different GO (graphene oxide) supporters used in the 2e-ORR for H_2O_2 production.[60] Graphene as an effective supporter could disperse the electron state of the active center in CoTCPP, facilitating the electron migration and adsorption of oxygen containing species. As a consequence, MOF@NG′ exhibited superior 2e-ORR performance, with an electron transfer

number of 2.24, low Tafel slope of 58 mV dec^{-1} and FE of 93.4% in 0.5 M H_2SO_4.

More recently, Wang *et al.*[61] reported a MZIF8/graphite felt support (GF) composite (denoted as MGF) for the 2e-ORR using a microwave assisted route (Fig. 8(a)). Ultra-tiny MZIF8 particles with a diameter of 20 nm were evenly dispersed on the surface of GF (Fig. 8(b) and (c)). X-ray photoelectron spectroscopy (XPS) measurements indicated the formation of N–Zn–O bonds between two components (Fig. 8(d)–(f)). Thanks to the facilitated adsorption of oxygen and water on the N–Zn–O active sites at a mild hydrophobic interface and microporous structure with facilitated reactant/product diffusion, high 2e$^-$ selectivities of 95% and 90% were achieved in 0.1 M KOH and 0.5 M Na_2SO_4, respectively, with the H_2O_2 yield increased by 191% compared to the sample prepared through self-growth of MZIF8 on GF (Fig. 8(g) and (h)).

The combination of MOFs and other functional materials provides MOF composites with enhanced conductivity and stability. Moreover, the synergism between different components offers additional physicochemical properties compared to individual components, resulting in higher activity and selectivity. Considering the huge number of MOFs and other

1092 | *Mater. Chem. Front.*, 2024, **8**, 1084–1100

This journal is © The Royal Society of Chemistry and the Chinese Chemical Society 2024

Fig. 8 (a) Schematic showing the synthesis process of MGF. TEM images of (b) MGF and (c) MZIF8. High-resolution XPS spectra of (d) N 1s, (e) O 1s and (f) Zn 2p for MGF. (g) H_2O_2 concentration over the reaction time at various solutions of MGF and GF: (g) pH = 7 (0.5 M Na_2SO_4), and (h) pH = 13 (0.1 M KOH). Copyright 2023, American Chemical Society.

functional materials, the development of MOF composite-based 2e-ORR electrocatalysts is still in its infancy.

3.3 MOF derivatives

Except for the direct use with or with combining other materials, MOFs can also serve as fascinating precursors/templates for fabricating derived functional materials including carbon, metal compounds and their hybrid materials *via* thermal and/or chemical treatments. Compared to pristine MOFs, MOF derivatives generally exhibit the advantages of high chemical stability and electronic conductivity, which are conducive to the 2e-ORR process. For instance, Liu and co-workers[62] reported MOF derived hierarchically porous carbon (HPC) with a high content of defects and sp^3-C, which can act as active sites for the absorption of OOH*, showing an excellent selectivity of 95% and a high H_2O_2 yield of 395.7 mol g_{cat}^{-1} h^{-1}. Through further incorporation of different heteroatoms into the carbon-based materials, the induced charge redistribution could produce more active sites.[63] Zhao et al.[64] synthesized F-doped porous carbon (FPC) by carbonization of MIL-53 (Al). Through systematic studies, it was found that the appropriate incorporation of F atoms into the carbon structure could optimize the active sites, and enhance the electrochemical activity and charge transfer, resulting in an improvement in the 2e-ORR performance. Compared to pure porous carbon materials, metal-doped carbon

materials have attracted more interest in the field of 2e-ORRs, in which metal atoms can be effectively dispersed onto the porous carbon substrates as highly active sites.[65,66] For example, Jia et al.[67] explored the 2e-ORR performances of metal/carbon electrocatalysts by using two MOFs with the same metal ion (Zn^{2+}) but different organic linkers, BDC or NH_2-BDC (BDC = 1,4-dicarboxybenzene or NH_2-BDC = 2-aminoterephthalic acid, Fig. 9(a)).

After heating under an argon atmosphere, most of the Zn in MOFs was evaporated, forming the nanosheet morphology (Fig. 9(b)). The active sites were characterized using Fourier-transformed (FT) curves (denoted as ZnO_3C or ZnN_4). The FT curves revealed two different coordination environments and the active sites of the Zn–N and Zn–O bonds (Fig. 9(f)). Based on the DFT calculations, the reduced electron density around Zn in ZnO_3C led to a lower d-band center than ZnN_4, altering the intermediate adsorption and offering a high selectivity toward the 2e-ORR (Fig. 9(g) and (h)). Therefore, the ZnO_3C showed a superior performance, with a near zero overpotential and Faraday efficiency of 90%. The H_2O_2 yield of about 350 mmol g_{cat}^{-1} h^{-1} in 0.1 M KOH was 3.5 times higher than Zn–N_4 (Fig. 9(c)–(e))

As a subclass of MOF, zeolitic imidazolate frameworks (ZIF) with a high N content are ideal precursors to synthesize various sing atom catalysts (SACs). For example, Wang et al. developed
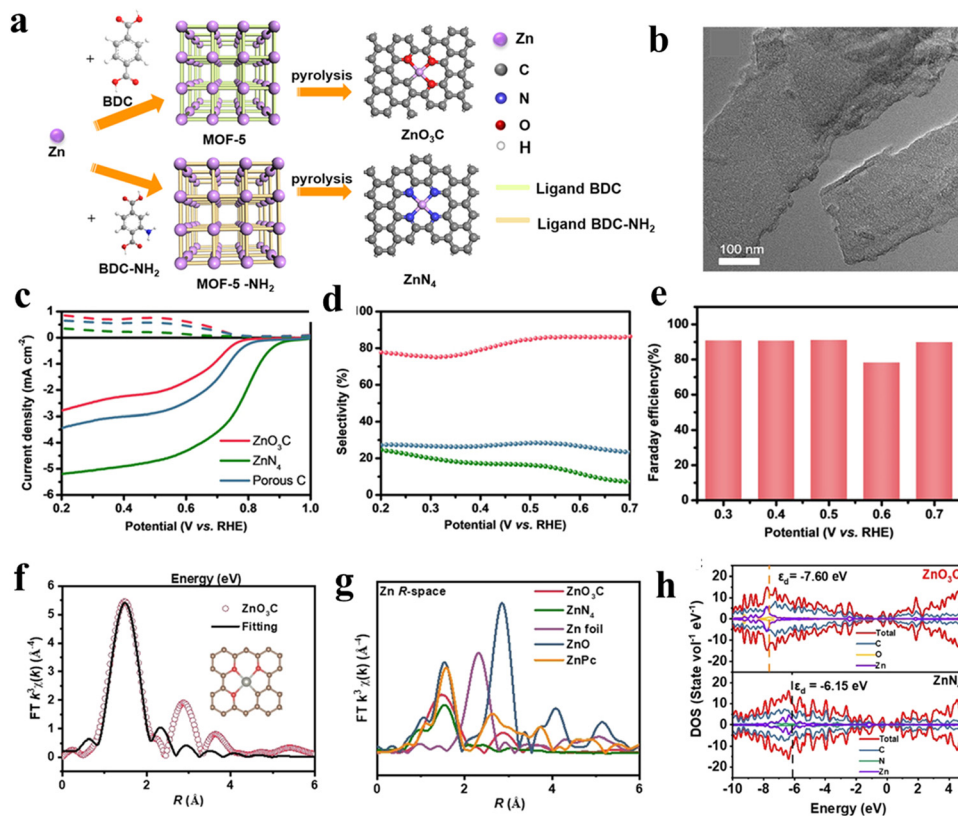
Fig. 9 (a) Schematic illustration of the fabrication route for ZnO_3C and ZnN_4 electrocatalysts. (b) TEM image of ZnO_3C. (c) LSV curves and (d) selectivity of ZnO_3C and ZnN_4 in 0.1 M KOH. (e) Faraday efficiency of ZnO_3C at different potentials. (f) Fourier-transformed (FT) curves of the Zn K-edge for ZnN_4, ZnO_3C, and the reference samples. (g) EXAFS fitting curves of ZnO_3C in *R* space. (h) Calculated DOS of ZnN_4 and ZnO_3C. Copyright 2016, WILEY-VCH.
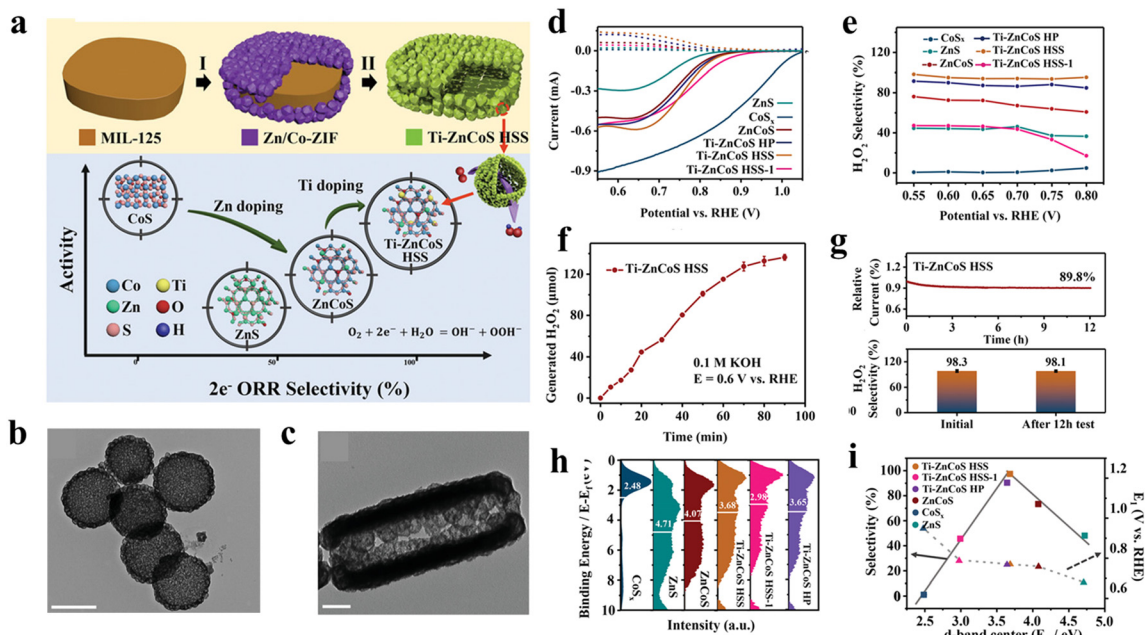
a MOF-engaged strategy to construct Pd SACs by directly pyrolyzing Pd doped ZIF-8 with different Pd/Zn ratios.[68] The optimized sample with a Pd/Zn mass ratio of 0.157 : 1 exhibited the best 2e-ORR performance with a selectivity of ~95%, onset potential of ~0.8 V and H_2O_2 production of ~30 mmol g_{cat}^{-1} h^{-1} in 0.1 M KOH. DFT calculations demonstrated that the active site Pd–N_4 was more favorable for the *–O bond breaking, resulting in the high performance. More recently, Wei and colleagues synthesized a SAC-based 2e-ORR electrocatalyst with an ultrahigh-loading Zn–N_3O SAC amount of 11.34 wt% by using ZIF-8 modified Zn^{2+} containing polypyrrole (PPy) as the precursors.[69] The unsymmetrical coordination environment of Zn–N_3O active sites was proved to modulate the charge redistribution toward the promoted absorption and desorption of intermediates OOH*, thus enhancing the 2e-ORR selectivity and activity. As a result, the excellent H_2O_2 performance with a selectivity of nearly 100%, high production of 248 mmol g_{cat}^{-1} h^{-1} and good stability was achieved.

Apart from carbon materials, MOF-derived transition metal chalcogenides (TMCs) have been demonstrated to be a promising type of 2e-ORR electrocatalyst. In 2022, Zhang *et al.*[71] reported a titanium-doped zinc–cobalt sulfide hollow superstructure (Ti–ZnCoS HSS) as an efficient 2e-ORR electrocatalyst by using a MOF-on-MOF heterostructure as the precursor. Specifically, a core–shell NH_2-MIL-125@ZnCo-ZIF hybrid MOF

was fabricated by growing ZnCo-ZIF nanocrystals on the surface of NH_2-MIL-125 (Fig. 10(a)). Through a subsequent sulfidation process, Ti–ZnCoS HSS was obtained, exhibiting an intricate hollow-on-hollow superstructure with small nanocages assembled around a large cake-like cavity (Fig. 10(b) and 10(c)). For comparison, ZnS, CoSx, ZnCoS and Ti–ZnCoS hollow particles were also prepared. Among these samples, Ti–ZnCoS HSS showed superior 2e-ORR performance with a high selectivity of ~98%, excellent activity (potential at 1 mA cm^{-2} of 0.774 V) and H_2O_2 production rate of 675 mmol h^{-1} g_{cat}^{-1} in 0.1 M KOH (Fig. 10(d) and (e)). Based on the valence band spectra test and DFT simulation, it was found that the polymetallic doping could alter the d-band center toward an optimized adsorption capability of OOH* intermediates, which is further evidenced by the volcano-type curve between selectivity and d band center value (Fig. 10(f) and (g)). Additionally, the hollow superstructure gave the electrocatalyst more abundant active sites and accelerated mass and electron transfer. By means of the synergistic d band center and superstructure engineering, the 2e-ORR performance was significantly improved (Fig. 10(h) and (i)).

The complete decomposition of MOFs into carbon materials or metal sulphides often leads to the serious destruction of MOFs with their intrinsic structural advantages sacrificed.[72] Recently, a partially controlled pyrolysis strategy was developed for partial conversion of the metal ions into functional objects

1094 | *Mater. Chem. Front.*, 2024, **8**, 1084–1100

This journal is © The Royal Society of Chemistry and the Chinese Chemical Society 2024

Fig. 10 (a) Illustration of the two-step synthesis of Ti–ZnCoS HSS and the 2e-ORR activity–selectivity of CoSx, ZnS, ZnCoS, and Ti–ZnCoS HSS. (b) and (c) TEM images of Ti–ZnCoS HSS. (d) LSV curves. (e) H_2O_2 selectivity of all samples in 0.1 M KOH. (f) Valence band spectra. (g) Relationship between selectivity/activity and d-band center. (h) Free-energy diagram for the ORR to H_2O_2. (i) Scheme presenting the 2e-ORR process over Ti–ZnCoS HSS. Copyright 2022, WILEY-VCH.

with the crystalline framework of MOFs partially retained by carefully controlling the thermal treatment conditions. For instance,

Huang *et al.*[73] reported the synthesis a series of MOF derivatives (MOF NSs-*T*, *T* = temperature) by using NiFe-BDC nanosheets as
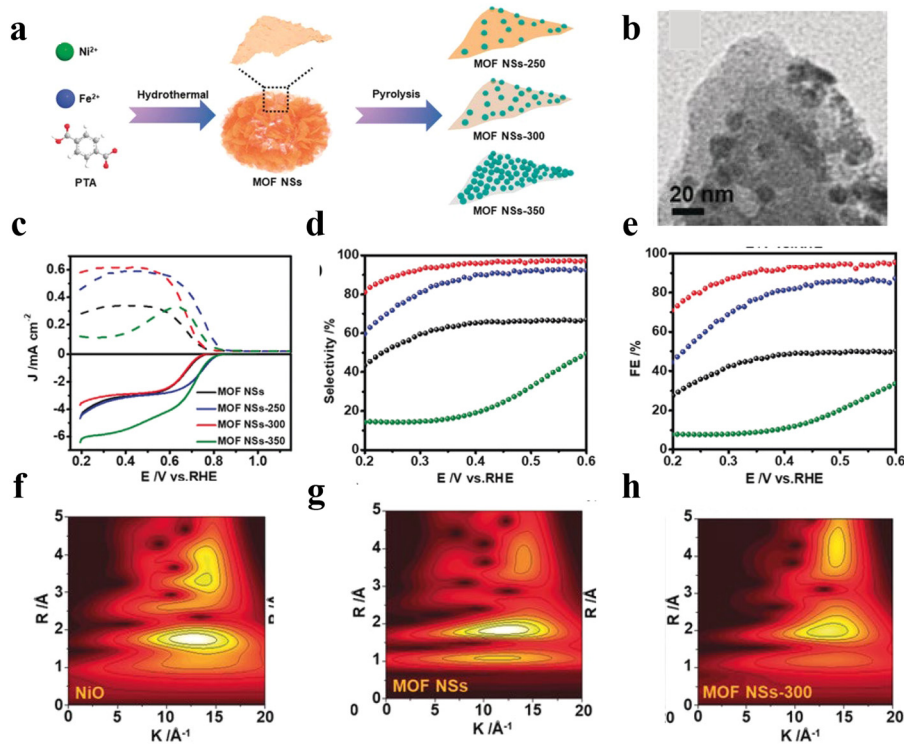
Fig. 11 (a) Schematic of the fabrication process of partially pyrolyzed MOF NSs. (b) TEM image of MOF NSs-300. (c) LSV curves of MOF NSs, MOF NSs-250, MOF NSs-300, and MOF NSs-350 in 0.1 M KOH. (d, e) Selectivity and FE% for different products in 0.1 M KOH. Wavelet transforms for the k^3-weighted Ni K-edge EXAFS signals of NiO (f), MOF NSs (g), and MOF NSs-300 (h). Copyright 2020, WILEY-VCH.

Table 1 Summary of the synthesis strategies and 2e-ORR performances of MOF-based electrocatalysts

Sample	Synthesis method	Selectivity (%)	Productivity (mol g_{cat}^{-1} h^{-1})	Electrolyte	Ref.
Zn-PBA	Solution precipitation	88	—	0.1 M KOH	52
Ni MOF NSs	Liquid–liquid interfacial reaction	98	0.08	0.1 M KOH	16
Cu-HHTP	Solvothermal method	95	0.79	0.1 M KOH	53
Br–Ni MOFs	Facile ion confinement strategy	90	0.596	0.1 M KOH	54
Ni_3HAB_2	Ions exchange strategy	95	0.51	0.1 M KOH	55
$Mg_3(HITP)_2$	Solvothermal method	90	0.05	0.1 M PBS	56
NiZn MOF	A facile one-step wet chemical method	90	—	0.1 M KOH	57
ZnCo-ZIF-C_3	Solution precipitation	92/100	3.8/4.35	0.1 M PBS/0.1 M KOH	44
MOF@NG'	Solvothermal method	—	—	0.5 M H_2SO_4	60
MGF	Microwave method	85/90	0.98/0.98	0.5 M Na_2SO_4/0.1 M KOH	61
HPC	Hydrothermal and carbonization	95/90	0.11	0.1 M Na_2SO_4/0.5 M H_2SO_4	62
FPC	Solvothermal method	97.5	0.792	0.05 M H_2SO_4	64
ZnO_3C	Solvothermal and carbonization	90	0.35	0.1 M KOH	67
Pd SACs	Pyrolysis	95	0.3	0.1 M KOH	68
Zn–N_3O SAC	Pyrolysis	100	0.248	0.1 M KOH	69
Ti–ZnCoS HSS	Sulfidation treatment	98	0.675	0.1 M KOH	70
MOF NSs-300	Hydrothermal thermal treatment	99	6.5	0.1 M KOH	72

the starting materials with various pyrolysis temperatures under an Ar atmosphere (Fig. 11(a)). At the optimized temperature, *in situ* generated NiO nanoparticles were uniformly anchored on MOF NSs (Fig. 11(b)), resulting in MOF NSs-300 with high activity, a high H_2O_2 selectivity of 99%, FE of 95% and high-yield rate of 6.5 mol g_{cat}^{-1} h^{-1} (Fig. 11(c)–(e)). Fourier transform (FT) EXAFS spectroscopy was performed to investigate the catalytic mechanism over MOF NS-300 (Fig. 11(f)–(h)). The results suggested that the unsaturated coordination environment of the Ni atom had more active sites for the adsorption of oxygen and the Fe in the MOF could modulate the coordination environment of Ni. The synergistic effect between NiO and NiFe MOFs thus optimized the binding with OOH*, reinforcing the activity and stability. Besides, the coordination unsaturated Ni atoms provided more open active sites for the adsorption of oxygen, further promoting the 2e-ORR to H_2O_2 production.

Compared to pristine MOFs and MOF composites, MOF derivatives generally possess superior conductivity and stability. The diversity of MOF precursors and conversion processes is conducive for the preparation of derived functional materials with tunable components. However, the harsh conditions during the conversion of MOFs often lead to the serious aggregation of metal ions/nodes and destruction of the pore structures of MOFs with a dramatic reduction in the specific surface area, impeding the active site utilization and mass transfer that are crucial in the 2e-ORR.

4. Conclusions and perspectives

In summary, this review provides a comprehensive overview of the recent advances of MOF-based materials as highly efficient electrocatalysts for 2e-ORRs (Table 1). Despite remarkable progress, the field of MOF-based 2e-ORR electrocatalysts is still in its infancy. There are numerous challenges that need to be overcome, some are listed below.

Rational design of the structure and composition of MOF-based electrocatalysts is still the central task for improving the 2e-ORR performance. Compared to the widely studied 2e-ORR electrocatalysts such as carbon-based materials, MOF-based electrocatalysts, especially pristine MOFs, are still rarely reported. The major challenges faced by MOFs are their relatively low stability and poor conductivity. To address the issue of stability, the design of MOFs with a strong bonding strength of metal–ligand coordination by assembling high-oxidation metal ions with carboxylate ligands, or soft metal ions with basic azolate ligands is an effective strategy. To improve the conductivity, constructing donor–acceptor interactions, introducing redox-matching units and mixed valency, or hybridizing conducive substrates (*e.g.* graphene, carbon nanotube) are highly promising methods. However, most of the reported MOF-based 2e-ORR electrocatalysts exhibited a micropore-dominated nature and solid structure, greatly limiting the active site exposure and mass transfer. To resolve these problems, introducing hierarchical pores (*e.g.* mesopore and macropore) is desired. Besides, the construction of complex architecture in MOF-based materials such as hollow, yolk–shell or open-frame-like structures is also promising. To this end, template-assistant routes including soft and hard templates and a selective etching strategy are recommended.[67]

From a compositional aspect, the current studies are mainly focused on mono- or bi-metal systems. Introducing more metal sites (more than two) into MOFs,[74,75] or even designing high-entropy MOFs, possibly benefits from further regulating the electronic state of electrocatalysts. For MOF derivatives, except for the reported carbon materials and metal sulphides, other functional components such as metal phosphides, metal nitrides, metal oxides and metal selenides are seldomly used in 2e-ORRs. At the level of hybrid materials, the conjugation of MOFs and their derivatives with other functional species with excellent electrochemical properties (*e.g.* metal sulphides,[76] metal oxides,[77] Mxene[78]) may provide new opportunities for building efficient 2e-ORR active sites, while related research is rare to date.

Besides, compared to the carbon-based materials, the poor conductivity and instability of MOF-based electrocatalysts

especially pristine MOFs in electrolyte severely restrict their rapid development in 2e-ORR electrocatalysis. To date, one of the primary strategies for enhancing the stability of MOF-based materials is to strengthen the bonding strength of metal–ligand coordination. For instance, some MOFs that consist of high-oxidation state metal ions and carboxylate ligands have been developed $(Zr_6O_4(OH)_8(H_2O)_4(CTTA)_{8/3})$. For the challenge of poor conductivity, some strategies have been developed such as redox-matching, donor–acceptor interactions and π-interactions.[79,80] These strategies can improve the stability and conductivity of MOFs to some extent.

Understanding of the electrocatalytic mechanism of MOF-based materials is also highly important. The use of advanced *in situ* characterizations (*e.g. in situ* electron microscope, IR spectra, XRD spectra, XPS spectra) to monitor the changes of morphology, crystal and chemical structures of MOFs and also the evolution of intermediate products during the 2e-ORR process is highly recommended.[81] High-throughput screening methods such as machine learning will provide powerful tools for predicting the performances of MOF-based materials and guide future electrocatalyst design.

To promote the practical applications of MOF-based 2e-ORR electrocatalysts, the stability of MOF-based materials needs to be further improved in a wide range of pH, especially in acidic media.

From the aspect of economics and energy efficiency, the synthesis process of many MOFs requires high-temperature hydro/solvothermal treatment with the use of expensive ligands. To promote their practical applications, the industrialization and commercialization of MOF materials using cheap ligands and energy-saving methods is the key, which have achieved impressive advances very recently. For example, over 10 kinds of inexpensive MOFs such as HKUST-1, MOF-5, ZIF-8 and ZIF-67 have been produced on a large scale by MOF Technologies and Strem Chemicals. Therefore, the design of efficient 2e-ORR electrocatalysts based on these MOFs is highly promising for H_2O_2 production. On the other hand, applying MOFs as catalysts with even relatively high costs for producing high-value-added chemicals is still attractive due to their fascinating properties and superior performances.

Overall, we have highlighted the current research achievements in the exciting field of MOF-based 2e-ORR electrocatalysts. Even though some challenges still exist, the rapid development of material science and electrochemistry is believed to produce many exciting outcomes with respect to the synthesis of MOF materials for H_2O_2 production in the near future.

Author contributions

The manuscript was collaboratively written by all authors. All authors have given their approval to the final version of the manuscript.

Conflicts of interest

The authors declare no conflict of interest.

Acknowledgements

Notes and references

1 R. Hage and A. Lienke, Applications of transition-metal catalysts to textile and wood-pulp bleaching, *Angew. Chem., Int. Ed.*, 2006, **45**, 206–222.

2 X. C. Wang, J. N. Jing, M. H. Zhou and R. Dewil, Recent advances in H_2O_2-based advanced oxidation processes for removal of antibiotics from wastewater, *Chin. Chem. Lett.*, 2023, **34**, 107621.

3 B. Puertolas, A. K. Hill, T. Garcia, B. Solsona and L. Torrente-Murciano, In-situ synthesis of hydrogen peroxide in tandem with selective oxidation reactions: A mini-review, *Catal. Today*, 2015, **248**, 115–127.

4 Y. C. Zeng and G. Wu, Electrocatalytic H_2O_2 generation for disinfection, *Chin. J. Catal.*, 2021, **42**, 2149–2163.

5 E. Brillas, I. Sires and M. A. Oturan, Electro-Fenton Process and Related Electrochemical Technologies Based on Fenton's Reaction Chemistry, *Chem. Rev.*, 2009, **109**, 6570–6631.

6 S. Fukuzumi and Y. Yamada, Hydrogen Peroxide used as a Solar Fuel in One-compartment fuel cells, *ChemElectroChem*, 2016, **3**, 1978–1989.

7 J. M. Campos-Martin, G. Blanco-Brieva and J. L. G. Fierro, Hydrogen peroxide synthesis: An outlook beyond the anthraquinone process, *Angew. Chem., Int. Ed.*, 2006, **45**, 6962–6984.

8 S. J. Freakley, Q. He, J. H. Harrhy, L. Liu, D. A. Crole, D. J. Morgan, E. N. Ntainjua, J. K. Edwards, A. F. Carley, A. Y. Borisevich, C. J. Kiely and G. J. Hutchings, Palladium-tin catalysts for the direct synthesis of H_2O_2 with high selectivity, *Science*, 2016, **351**, 965–968.

9 R. B. Rankin and J. Greeley, Trends in selective hydrogen peroxide production on transition metal surfaces from first principles, *ACS Catal.*, 2012, **2**, 2664–2672.

10 D. W. Flaherty, Direct synthesis of H_2O_2 from H_2 and O_2 on Pd catalysts: current understanding, outstanding questions, and research needs, *ACS Catal.*, 2018, **8**, 1520–1527.

11 Y. H. Li, Q. Y. Li, H. Q. Wang, L. Zhang, D. P. Wilkinson and J. J. Zhang, Recent Progresses in Oxygen Reduction Reaction Electrocatalysts for Electrochemical Energy Applications, *Electrochem. Energy Rev.*, 2019, **2**, 518–538.

12 T. P. Fellinger, F. Hasche, P. Strasser and M. Antonietti, Mesoporous nitrogen-doped carbon for the electrocatalytic synthesis of hydrogen peroxide, *J. Am. Chem. Soc.*, 2012, **134**, 4072–4075.

13 J. S. Jirkovsky, I. Panas, E. Ahlberg, M. Halasa, S. Romani and D. Schiffrin, Single atom hot-spots at Au-Pd nanoalloys for electrocatalytic H_2O_2 production, *J. Am. Chem. Soc.*, 2011, **133**, 19432–19441.

14 Z. Y. Lu, G. X. Chen, S. Siahrostami, Z. H. Chen, K. Liu, J. Xie, L. Liao, T. Wu, D. C. Lin, Y. Y. Liu, T. F. Jaramillo, J. K. Nørskov and Y. Cui., High-efficiency oxygen reduction to hydrogen peroxide catalysed by oxidized carbon materials, *Nat. Catal.*, 2018, **1**, 156–162.

15 E. Y. Jung, H. J. Shin, B. H. Lee, V. Efremov, S. Y. Lee, H. S. Lee, J. Kim, W. H. Antink, S. B. Park, K. S. Lee, S. P. Cho, J. S. Yoo, Y. E. Sung and T. Hyeon, Atomic-level tuning of Co–N–C catalyst for high-performance electrochemical H_2O_2 production, *Nat. Mater.*, 2020, **19**, 436–442.

16 S. K. Sahoo, Y. J. Ye, S. Lee, J. Park, H. Lee, J. Lee and J. W. Han, Rational design of TiC-Supported single-atom electrocatalysts for hydrogen evolution and selective oxygen reduction reactions, *ACS Energy Lett.*, 2019, **4**, 126–132.

17 M. J. Wang, X. Dong, Z. D. Meng, Z. W. Hu, Y. G. Lin, C. K. Peng, H. S. Wang, C. W. Pao, S. Y. Ding, Y. Y. Li, Q. Shan and X. Q. Huang, An Efficient interfacial synthesis of two-dimensional metal-organic framework nanosheets for electrochemical hydrogen peroxide production, *Angew. Chem., Int. Ed.*, 2021, **60**, 11190–11195.

18 L. L. Zhang, S. Y. Jiang, W. Ma and Z. Zhou, Oxygen reduction reaction on Pt-based electrocatalysts: Four-electron *vs.* two-electron pathway, *Chin. J. Catal.*, 2022, **43**, 1433–1443.

19 S. Siahrostami, A. Verdaguer-Casadevall, M. Karamad, D. Deiana, P. Malacrida, B. Wickman, M. Escudero-Escribano, E. A. Paoli, R. Frydendal, T. W. Hansen, I. Chorkendorff, I. Stephens, I. Stephens and J. Rossmeisl, Enabling direct H_2O_2 production through rational electrocatalyst design, *Nat. Mater.*, 2013, **12**, 1137–1143.

20 Y. Y. Sun, I. Sinev, W. Ju, A. Bergmann, S. Dresp, S. Kühl, C. Spöri, H. Schmies, H. Wang, D. Schmies, B. Paul, R. Paul, R. Kraehnert, B. R. Cuenya and P. Strasser, Efficient electrochemical hydrogen peroxide production from molecular oxygen on nitrogen-doped mesoporous carbon catalysts, *ACS Catal.*, 2018, **8**, 2844–2856.

21 W. W. Zhao, P. Bothra, Z. Y. Lu, Y. B. Li, L. P. Mei, K. Liu, Z. H. Zhao, G. X. Chen, S. Back, S. Siahrostami, A. Kulkarni, J. Nørskov, M. Bajdich and Y. Cui, Improved oxygen reduction reaction activity of nanostructured CoS_2 through electrochemical tuning, *ACS Appl. Energy Mater.*, 2019, **2**, 8605–8614.

22 H. Y. Sheng, E. Hermes, X. H. Yang, D. W. Ying, A. N. Janes, W. J. Li, J. R. Schmidt Song and S. Jin, Electrocatalytic production of H_2O_2 by selective oxygen reduction using Earth-abundant cobalt pyrite (CoS_2), *ACS Catal.*, 2019, **258**, 8433–8442.

23 J. Lee, O. K. Farha, J. Roberts, K. Schedit, S. Nguyen and J. Hupp, Metal-organic framework materials as catalysts, *Chem. Soc. Rev.*, 2009, **38**, 1450–1459.

24 W. Xia, A. Mahmood, R. Q. Zou and Q. Xu, Metal-organic frameworks and their derived nanostructures for electrochemical energy storage and conversion, *Energy Environ. Sci.*, 2015, **8**, 1837–1866.

25 X. F. Lu, Y. J. Fang, D. Y. Luan and X. W. Lou, Metal–Organic Frameworks derived functional materials for electrochemical energy storage and conversion: A mini review, *Nano Lett.*, 2021, **21**, 1555–1565.

26 W. R. Cheng, X. F. Lu, D. Y. Luan and X. W. Lou, NiMn-based bimetal–organic framework nanosheets supported on multi-channel carbon fibers for efficient oxygen electrocatalysis, *Angew. Chem., Int. Ed.*, 2020, **59**, 18234–18239.

27 X. F. Lu, P. Q. Liao, J. W. Wang, J. X. Wu, X. W. Chen, C. T. He, J. P. Zheng, G. R. Li and X. M. Chen, An alkaline-stable, metal hydroxide mimicking metal–organic framework for efficient electrocatalytic oxygen evolution, *J. Am. Chem. Soc.*, 2016, **138**, 8336–8339.

28 S. L. Zhao, Y. Wang, J. C. Dong, C. T. He, H. J. Yin, P. F. An, K. Zhao, X. F. Zhang, C. Chao, L. J. Zhang, J. W. Lv, J. X. Wang, J. X. Wang, J. Q. Zhang, A. Khattak, N. Khan, Z. X. Wei, J. Zhang, S. Q. Liu, H. J. Zhao and Z. Y. Tang, Ultrathin metal-organic framework nanosheets for electrocatalytic oxygen evolution, *Nat. Energy*, 2016, **1**, 1–10.

29 J. Q. Shen, P. Q. Liao, D. D. Zhou, C. T. He, J. X. Wu, W. X. Zhang, J. P. Zhang and X. M. Chen, *et al.*, Modular and stepwise synthesis of a hybrid metal-organic framework for efficient electrocatalytic oxygen evolution, *J. Am. Chem. Soc.*, 2017, **139**, 1778–1781.

30 M. C. Gonzalez, A. Turkiewicz, L. Darago, K. Bustillo, F. Grandjean, G. Long and J. R. Long, Confinement of atomically-defined metal halide sheets in a metal–organic framework, *Nature*, 2019, **258**, 64–68.

31 Z. R. Tao, J. X. Wu, Y. J. Zhao, M. Xu, W. Q. Tang, Q. H. Zhang, L. Gu, D. H. Liu and Z. Y. Gu, Untwisted restacking of two-dimensional metal-organic framework nanosheets for highly selective isomer separations, *Nat. Commun.*, 2019, **10**, 2911.

32 L. Yang, X. F. Zeng, W. C. Wang and D. P. Cao, Recent progress in MOF-derived, heteroatom-doped porous carbons as highly efficient electrocatalysts for oxygen reduction reaction in fuel cells, *Adv. Funct. Mater.*, 2018, **28**, 1704537.

33 X. F. Lu, B. Y. Xia, S. Q. Zang and D. Lou, Metal-organic frameworks based electrocatalysts for the oxygen reduction reaction, *Angew. Chem., Int. Ed.*, 2020, **59**, 4634–4650.

34 Z. P. Wu, X. F. Lu, S. Q. Zang and X. W. Lou, Non-noble-metal-based electrocatalysts toward the oxygen evolution reaction, *Adv. Funct. Mater.*, 2020, **30**, 1910274.

35 X. D. Wen and J. Q. Guan, Recent progress on MOF-derived electrocatalysts for hydrogen evolution reaction, *Appl. Mater. Today*, 2019, **16**, 146–168.

36 Y. J. Zhao, L. L. Zheng, D. Jiang, W. Xia, X. T. Xu, Y. Yamauchi, J. P. Ge and J. Tang, Nanoengineering metal-organic framework-based materials for use in electrochemical CO_2 reduction reactions, *Small*, 2021, **17**, 2006590.

37 I. E. Khalil, C. Xue, W. J. Liu, X. H. Li, Y. Shen, S. Li, W. N. Zhang and F. W. Huo, The role of defects in metal-organic frameworks for nitrogen reduction reaction: when defects switch to features, *Adv. Funct. Mater.*, 2021, **31**, 2010052.

38 S. Yang, A. Verdaguer-Casadevall, L. Arnarson, L. Silvioli, V. Čolić, R. Frydendal, J. Rossmeisl, I. Chorkendorff and I. Stephens, Toward the decentralized electrochemical production of H_2O_2: A focus on the catalysis, *ACS Catal.*, 2018, **8**, 4064–4081.

39 Y. Y. Jiang, P. J. Ni, C. X. Chen, Y. Z. Lu, P. Yang, B. Kong, A. Fisher and X. Wang, Selective electrochemical H_2O_2 production through two-electron oxygen electrochemistry, *Adv. Energy Mater.*, 2018, **8**, 1801909.

40 Y. Jiao, Y. Zheng, M. T. Jaroniec and S. Z. Qiao, Design of electrocatalysts for oxygen- and hydrogen-involving energy conversion reactions, *Chem. Soc. Rev.*, 2015, **44**, 2060–2086.

41 Y. Y. Sun, L. Han and P. Strasser, A comparative perspective of electrochemical and photochemical approaches for catalytic H_2O_2 production, *Chem. Soc. Rev.*, 2020, **49**, 6605–6631.

42 C. H. Choi, H. C. Kwon, S. Yook, H. Shin, H. Kim and M. Choi, Hydrogen peroxide synthesis *via* enhanced two-electron oxygen reduction pathway on carbon-coated Pt surface, *J. Phys. Chem. C*, 2014, **118**, 30063–30070.

43 X. H. Zhao and Y. Y. Liu, Origin of selective production of hydrogen peroxide by electrochemical oxygen reduction, *J. Am. Chem. Soc.*, 2021, **143**, 9423–9428.

44 C. Q. Zhang, L. Yuan, C. Liu, Z. M. Li, Y. Y. Zou, X. C. Zhang, Y. Zhang, Z. Q. Zhang, G. F. Wei and C. Z. Yu, Crystal engineering enables cobalt-based metal-organic frameworks as high-performance electrocatalysts for H_2O_2 Production, *J. Am. Chem. Soc.*, 2023, **145**, 7791–7799.

45 R. Sanchis-Gual, A. S. Silva, M. Coronado-Puchau, T. Otero, G. Abellán and E. Coronado, Improving the onset potential and Tafel slope determination of earth-abundant water oxidation electrocatalysts, *Electrochim. Acta*, 2021, **388**, 138613.

46 A. Speelman, J. Gerken, S. Heins, E. Wiedner, S. Stahl and A. Appel, Determining the Overpotential for a Molecular Electrocatalyst, *Energy Environ. Sci.*, 2014, **4**, 630–633.

47 U. A. Paulus, T. J. Schmidt, H. A. Gasteiger and R. Behm, Oxygen reduction on a high-surface area Pt/Vulcan carbon catalyst: a thin-film rotating ring-disk electrode study, *J. Electroanal. Chem.*, 2001, **495**, 134–145.

48 J. H. Baek, T. M. Gill, H. Abroshan, S. Park, X. J. Shi, J. Nørskov, H. S. Jung, S. Siahrostami and X. L. Zheng, Selective and Efficient Gd-Doped $BiVO_4$ Photoanode for Two-Electron Water Oxidation to H_2O_2, *ACS Energy Lett.*, 2019, **4**, 720–728.

49 M. H. Shao, P. Liu and R. R. Adzic, Superoxide anion is the intermediate in the oxygen reduction reaction on platinum electrodes, *J. Am. Chem. Soc.*, 2006, **128**, 7408–7409.

50 M. Liu, N. Li, S. F. Cao, X. M. Wang, X. Q. Lu, L. J. Kong, Y. H. Xu and X. H. Xu, A "pre-constrained metal twins" strategy to prepare efficient dual-metal-atom catalysts for cooperative oxygen electrocatalysis, *Adv. Mater.*, 2022, **34**, 2107421.

51 J. J. Mao, L. F. Yang, P. Yu, X. W. Wei and L. Q. Mao, Electrocatalytic four-electron reduction of oxygen with Copper (II)-based metal-organic frameworks, *Electrochem. Commun.*, 2012, **19**, 29–31.

52 M. Q. Ren, J. C. Lei, J. B. Zhang, B. Yakobson and J. Tour, Tuning metal elements in open frameworks for efficient oxygen evolution and oxygen reduction reaction Catalysts, *ACS Appl. Mater. Interfaces*, 2021, **13**, 42715–42723.

53 X. Sun, Y. Li, H. Su, X. X. Zhang, Y. Z. Xu, W. L. Xu, M. H. Liu, W. R. Cheng and Q. H. Liu, Dissecting

54 M. Liu, Y. Li, Z. Qi, H. Su, W. R. Cheng, W. L. Zhou, H. Zhang, X. Sun, X. X. Zhang, Y. Z. Xu, Y. Jiang, Q. H. Liu and S. Q. Wei, Self-nanocavity-confined halogen anions boosting the high selectivity of the two-electron oxygen reduction pathway over Ni-Based MOFs, *J. Phys. Chem. Lett.*, 2021, **12**, 8706–8712.

55 R. D. Ross, H. Sheng, Y. Ding, A. Janes, D. Feng, J. Schmidt, C. Segre and S. Jin, Operando elucidation of electrocatalytic and redox mechanisms on a 2D metal organic framework catalyst for efficient electrosynthesis of hydrogen peroxide in neutral media, *J. Am. Chem. Soc.*, 2022, **144**, 15845–15854.

56 K. Dong, J. Liang, Y. Wang, L. C. Zhang, Z. Q. Xu, S. J. Sun, Y. S. Luo, T. S. Li, Q. Liu, N. Li, B. Tang, A. A. Alshehri, Q. Li, D. W. Ma and X. P. Sun, Conductive two-dimensional magnesium metal–organic frameworks for high-efficiency O_2 electroreduction to H_2O_2, *ACS Catal.*, 2022, **12**, 6092–6099.

57 M. Liu, H. Su, W. Cheng, F. F. Yu, Y. L. Li, W. L. Zhou, H. Zhang, X. Sun, X. X. Zhang, S. Q. Wei and Q. L. Liu, Synergetic dual-ion centers boosting metal organic framework alloy catalysts toward efficient two electron oxygen reduction reaction, *Small*, 2022, **18**, 2202248.

58 Y. P. Wu, W. Zhou, J. Zhao, W. W. Dong, Y. Q. Lan, D. S. Li, C. H. Sun and X. H. Bu, Surfactant-assisted phase-selective synthesis of new cobalt MOFs and their efficient electrocatalytic hydrogen evolution reaction, *Angew. Chem., Int. Ed.*, 2017, **56**, 13001–13005.

59 H. B. Aiyappa, P. Wilde, T. Quast, J. Masa, C. Andronescu, Y. T. Chen, M. Muhler, R. Fischer and W. Schuhmann, Oxygen evolution electrocatalysis of a single MOF-derived composite nanoparticle on the tip of a nanoelectrode, *Angew. Chem., Int. Ed.*, 2019, **58**, 8927–8931.

60 B. Liu, K. Vellingiri, S.-H. Jo, P. Kumar, Y. S. Ok and K. Kim, Recent advances in controlled modification of the size and morphology of metal-organic frameworks, *Nano Res.*, 2018, **11**, 4441–4467.

61 G. Wang, Z. Bao, S. Zhang, S. J. Zhang, Y. N. Li, X. G. Peng, L. Ding, Y. F. Li, X. N. Li and J. G. Wang, Self-growing MZIF8/GDE bonding by N–Zn–O boosts electrochemical oxygen reduction to H_2O_2, *ACS Sustainable Chem. Eng.*, 2023, **11**, 1610–1617.

62 Y. M. Liu, X. Quan, X. F. Fan, H. Wang and S. Chen, High-yield electrosynthesis of hydrogen peroxide from oxygen reduction by hierarchically porous carbon, *Angew. Chem., Int. Ed.*, 2015, **54**, 6837–6841.

63 S. Xu, Y. Gao, T. Liang, L. P. Zhang and B. Wang, N, O-coupling towards the selectively electrochemical production of H_2O_2, *Chin. Chem. Lett.*, 2022, **33**, 5152–5157.

64 K. Zhao, Y. Su, X. Quan, Y. M. Liu, S. Chen and H. T. Yu, Enhanced H_2O_2 production by selective electrochemical reduction of O_2 on fluorine-doped hierarchically porous carbon, *J. Catal.*, 2018, **357**, 118–126.

65 X. Cui, L. Zhong, X. Zhao, J. X. Xie, D. Q. He, X. Yang, K. L. Lin, H. Wang and L. Niu, Ultrafine Co nanoparticles

π-conjugated covalent-coupling over conductive MOFs toward efficient two-electron oxygen reduction, *Appl. Catal., B*, 2022, **317**, 121706.

confined in nitrogen-doped carbon toward two-electron oxygen reduction reaction for H_2O_2 electrosynthesis in acidic media, *Chin. Chem. Lett.*, 2023, **34**, 108291.

66 Y. Wang, E. Luo, X. Wang, Q. L. Meng, J. J. Ge, C. P. Liu and W. Xing, Fe, Cu-codoped metal-nitrogen-carbon catalysts with high selectivity and stability for the oxygen reduction reaction, *Chin. Chem. Lett.*, 2021, **32**, 506–510.

67 Y. L. Jia, Z. Q. Xue, J. Yang, Q. L. Liu, J. H. Xian, Y. C. Zhong, Y. M. Sun, X. X. Zhang, Q. H. Liu, D. X. Yao and G. Q. Li, Tailoring the electronic structure of an atomically dispersed zinc electrocatalyst: coordination environment regulation for high selectivity oxygen reduction, *Angew. Chem., Int. Ed.*, 2022, **61**, e202110838.

68 N. Wang, X. H. Zhang, R. Zhang, S. Yu, Z. Levell, C. Y. Wang, S. B. Ma, P. C. Zou, L. L. Han, J. Y. Qin, L. Ma, Y. Y. Liu and H. L. Xin, Highly selective oxygen reduction to hydrogen peroxide on a carbon-supported single-atom Pd electrocatalyst, *ACS Catal.*, 2022, **12**, 4156–4164.

69 G. Y. Wei, X. P. Liu, Z. W. Zhao, C. B. Men, Y. Ding and S. Y. Gao, Constructing ultrahigh-loading unsymmetrically coordinated $Zn-N_3O$ single-atom sites with efficient oxygen reduction for H_2O_2 production, *Chem. Eng. J.*, 2023, **455**, 140721.

70 S. Yao, T. Huang, H. Fang, J. M. Yu, M. D. Meganathan, Z. X. Cui and X. X. Yuan, Cobalt sulfides as efficient catalyst towards oxygen reduction reactions, *Chin. Chem. Lett.*, 2020, **31**, 530–534.

71 C. Q. Zhang, R. H. Lu, C. Liu, J. Y. Lu, Y. Y. Zou, L. Yuan, J. Wang, G. Z. Wang, Y. Zhao and C. Z. Yu, Trimetallic Sulfide Hollow Superstructures with Engineered d-Band Center for Oxygen Reduction to Hydrogen Peroxide in Alkaline Solution, *Adv. Sci.*, 2022, **9**, 202100099.

72 X. L. Wang, H. Xiao, A. Li, Z. Li, S. J. Liu, Q. H. Zhang, Y. Gong, L. R. Zheng, Y. Q. Zhu, C. Chen, D. S. Wang, Q. Peng, L. Gu, X. D. Han, J. Li and Y. D. Li, Constructing $NiCo/Fe_3O_4$ heteroparticles within MOF-74 for efficient oxygen evolution reactions, *J. Am. Chem. Soc.*, 2018, **140**, 15336–15341.

73 M. J. Wang, N. Zhang, Y. G. Feng, Z. W. Hu, Q. Shao and X. Q. Huang, Partially pyrolyzed binary metal-organic framework nanosheets for efficient electrochemical hydrogen peroxide synthesis, *Angew. Chem., Int. Ed.*, 2020, **59**, 14373–14377.

74 J. J. Yu, X. Wang, L. Chen, G. H. Lu, G. S. Lu, X. F. Xie, Y. Wang and J. Sun, Enhanced adsorption and visible-light photocatalytic degradation of toluene by CQDs/UiO-66 MOG with hierarchical pores, *Chem. Eng. J.*, 2022, **435**, 135033.

75 J. Li, T. Bao, C. Q. Zhang, H. Song, Y. Y. Zou, L. Yuan, Y. M. Xi, C. Z. Yu and C. Liu, A general strategy for direct growth of yolk-shell MOF-on-MOF hybrids, *Chem. Eng. J.*, 2023, **472**, 144926.

76 W. D. Zhou, Z. Q. Xue, Q. L. Liu, Y. L. Li and G. Q. Li, Trimetallic MOF-74 Films Grown on Ni Foam as Bifunctional Electrocatalysts for Overall Water Splitting, *ChemSusChem*, 2020, **13**, 5647–5653.

77 D. S. Raja, C. L. Huang, Y. A. Chen, Y. M. Choi and S. Lu, Composition-balanced trimetallic MOFs as ultra-efficient electrocatalysts for oxygen evolution reaction at high current densities, *Appl. Catal., B*, 2020, **279**, 119375.

78 H. Xu, J. Cao, C. Shan, B. K. Wang, P. X. Xi, W. S. Liu and Y. Tang, MOF-derived hollow CoS decorated with CeOx nanoparticles for boosting oxygen evolution reaction electrocatalysis, *Angew. Chem., Int. Ed.*, 2018, **57**, 8654–8658.

79 Y. Yang, Z. Y. Lin, S. Q. Gao, J. W. Su, Z. Y. Lun, G. L. Xia, J. T. Chen, R. R. Zhang and Q. W. Chen, Tuning electronic structures of nonprecious ternary alloys encapsulated in graphene layers for optimizing overall water splitting activity, *ACS Catal.*, 2017, **7**, 469–479.

80 Y. L. Wang, J. Song and W. Y. Wong, Constructing 2D sandwich-like MOF/MXene heterostructures for durable and fast aqueous zinc-ion batteries, *Angew. Chem., Int. Ed.*, 2023, **62**, e202218343.

81 B. M. Weckhuysen, Preface: recent advances in the in-situ characterization of heterogeneous catalysts, *Chem. Soc. Rev.*, 2010, **39**, 4557–4559.